

Measurement and modelling of intensity dependent absorption and transit relaxation on the cesium D₁ line

J Sagle, R K Namiotka and J Huennekens

Department of Physics, Lehigh University, 16 Memorial Drive East, Bethlehem PA 18015, USA

Received 18 December 1995

Abstract. The intensity dependent absorption was measured on the D₁ line ($6S_{1/2} \rightarrow 6P_{1/2}$ transition) in atomic cesium. The magnetic field applied to the vapour and the spatial cross section of the laser beam were controlled and varied during data collection. A three-level rate equation model is presented in an attempt to explain the results. We show that this well known approach does not successfully model the data obtained in the absence of a magnetic field. Hence, a more complex and complete model that explicitly includes all of the hyperfine magnetic sublevels (a multilevel model) is presented. This approach accurately models all of the data collected. The good agreement between this model and the data allows the determination of the transit relaxation rate (due to atomic time of flight through the laser beam), $\Gamma_1 = (1.13 \pm 0.20)v_{\text{rms}}/D$, where v_{rms} is the two-dimensional root-mean-squared speed of the atom and D is the FWHM of the Gaussian laser beam spatial profile.

1. Introduction

The basis for many nonlinear optical phenomena is the nonlinear response produced by the saturation of atomic transitions. This saturation is commonly described in terms of an intensity dependent absorption coefficient α and quantified by a saturation intensity I_{sat} . Theoretical models of these phenomena include derivations of equations describing the intensity dependent absorption for both homogeneously and inhomogeneously broadened optical transitions, as well as the saturation intensity of two-level atoms [1–4]. It is also well known that three-level systems may display greatly reduced saturation intensities [2]. A number of measurements of saturation intensity have been carried out in atomic vapours, usually for the purpose of applying the values obtained to saturation spectroscopy studies [5, 6]. However, to the best of our knowledge, the literature contains no detailed comparison of absolute theoretical and experimental intensity dependent absorption. Here, we present data showing intensity dependent absorption on the cesium D₁ line. We compare these data with a three-level model for the absorption that includes Doppler broadening of the transition, the Gaussian transverse spatial profile of the laser beam, and beam attenuation over the length of the cesium cell. We demonstrate the effect of transit relaxation on the three-level saturation intensity by varying this transit time through changes in the size of the beam cross section. Also, by manipulating the magnetic field, we show that the three-level model often is inadequate. Thus, we present a more complete model that explicitly includes all of the hyperfine magnetic sublevels (a multilevel model) and explains all of the experimental data. The good agreement between model and measurements in all cases supports our use and calculation of an effective transit relaxation rate and provides a measured uncertainty for this rate. We compare this calculation and measured uncertainty with several other theoretical estimates of effective transit relaxation rate coefficients.

2. Experiment

The experiment was performed using a sealed cylindrical Pyrex cell of length $L = 6.9$ cm and diameter 2.1 cm containing pure cesium with no buffer gas. The cell temperature T (room temperature) was monitored with a thermocouple and kept constant to within 0.5°C throughout the experiment. The cell was located at the centre of three pairs of Helmholtz coils with coil radii $r_x = 12.1$ cm, $r_y = 14.6$ cm, and $r_z = 9.5$ cm. The magnetic field at the centre of these coils was measured using a transverse Hall effect probe and Gaussmeter (Bell model 640).

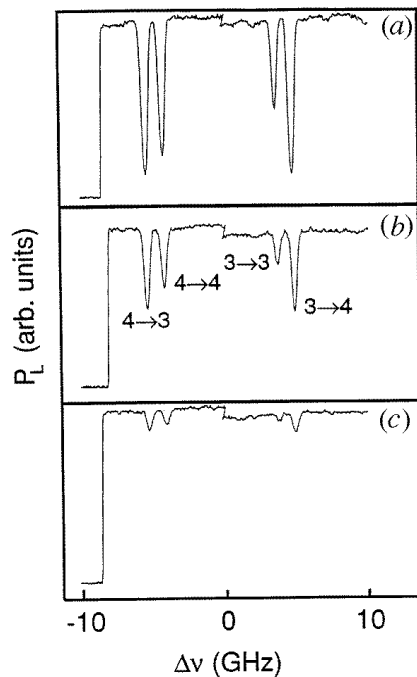


Figure 1. Transmitted signal against laser frequency. The transmitted laser power P_L was collected using a photomultiplier tube, as the laser (with a beam spatial profile FWHM of $D = 0.55 \pm 0.05$ mm) was scanned across the cesium $6S_{1/2} \rightarrow 6P_{1/2}$ transition. The laser beam was blocked at the beginning of each scan to determine a baseline. The discontinuity in the middle of each scan results from the reset of the laser's Brewster plate after scanning a 10 GHz segment. The four absorption dips visible in each spectrum result from the hyperfine structure. We label each transition as $F \rightarrow F'$, where F and F' are the quantum numbers of the ground- and excited-state hyperfine levels coupled by the laser. Incident intensities are (a) $P_0 = 2.1$ nW, (b) $P_0 = 22$ μW , and (c) $P_0 = 166$ μW . Note the decrease in transmittance with increasing incident intensity as the transitions saturate.

An argon-ion laser pumped, single-mode, tunable titanium-sapphire laser (coherent model 899-29) was used to study the intensity dependent absorption of the cesium $6S_{1/2} \rightarrow 6P_{1/2}$ transition (D_1 line). This laser beam was directed through the length of the cell (in the \hat{y} direction) and was linearly polarized in the \hat{z} direction. The laser beam spatial profile was recorded using a two-dimensional diode array (Spectra Source Instruments model LYNXX PC), hence allowing the accurate determination of the beam's Gaussian full width at half maximum (FWHM), D . This FWHM at the cell position was adjusted by placing different lenses in the beam path. The incident laser power (for powers greater than

1 μW) was measured with the laser tuned off resonance using an Ophir (model PD2-A) power meter placed after the cell. This reading was corrected for the attenuation caused by the Pyrex exit window. The incident power was varied using a variable neutral density filter and two polarizing cubes. The second cube was set to pass light linearly polarized in the \hat{z} direction and then never adjusted over the course of the experiment, thus preserving the laser polarization for all incident powers. The frequency dependent transmitted laser power was measured using a chilled photomultiplier (Hamamatsu R636) with output sent to a lock-in amplifier (Stanford Research Systems model SR510) and then to a computer running the coherent autoscan laser frequency scanning software. The amplitude of the off-resonance photomultiplier signal was used to calibrate incident powers below the 1 μW reading threshold of the power meter.

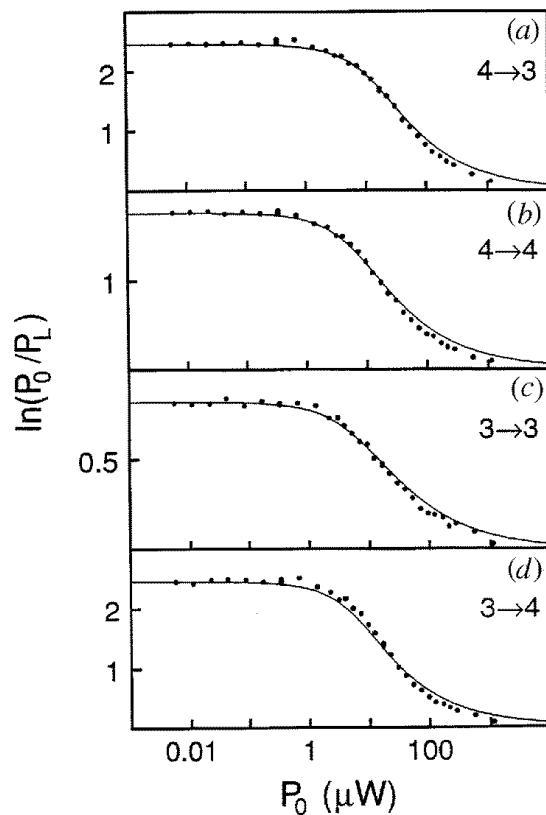


Figure 2. Effective line centre optical depth $\ln(P_0/P_L)$ against incident power P_0 . Each of the four $6S_{1/2}(F) \rightarrow 6P_{1/2}(F')$ hyperfine transitions (labelled as $F \rightarrow F'$) were analysed using data collected in set no 4. The magnetic field transverse to the laser polarization axis was $B_x = (1.10 \pm 0.02)$ G. The experimental data appear as circles, while the results of the three-level model presented in section 3.1 of the paper appear as full curves. The multilevel model results of sections 3.2 and 3.3 (including magnetic field mixing) are identical with the three-level model results. Note the good agreement between experiment and theory in all four cases. Results from data set no 3 are comparable in all respects.

Absorption data were collected under four different sets of conditions, listed in table 1. Each data set consists of approximately 35 absorption scans across the cesium D_1 resonance line. Each scan within a given set was collected under the same conditions, except for the incident power, which was varied from a few mW to a few nW. The magnetic fields B_y and B_z were set to $B_y = (0 \pm 5)$ mG and $B_z = (0 \pm 10)$ mG using the Helmholtz coils. Sample scans demonstrating the saturation of the four hyperfine transitions are shown in figure 1. Each of the four transitions was analysed independently. For a given transition, each scan was analysed to find $\ln(P_0/P_L)$, where P_0/P_L is the ratio of incident power to that transmitted through a length L of vapour at line centre. The transmitted signal is simply the signal minimum for the transition, while the incident signal is found by interpolating

the off resonance signals to the frequency of the signal minimum. These data were plotted versus the measured incident laser power P_0 and are shown in figures 2 and 3 for two of the data sets.

Table 1. Conditions under which the four experimental data sets were obtained.

Set no	T (± 0.5 °C)	D (mm) ($\pm 10\%$)	B_x (mG)
1	24.0	1.10	0 ± 5
2	24.0	0.55	0 ± 5
3	25.5	0.45	1100 ± 20
4	25.5	1.30	1100 ± 20

3. Theoretical results and comparison to experiment

3.1. Three-level model

A simple prediction of the intensity dependent absorption can be made by considering either a three-level rate equation or density matrix model. The density matrix approach properly accounts for coherence effects, but does not easily allow incorporation of degenerate magnetic sublevels. However, both the rate equation and density matrix approaches yield the same intensity dependent absorption in cases where each level is considered to be non-degenerate and where only two-levels are coupled by the laser at any given time. Due to the presence of degenerate sublevels in this experiment, we choose to use the rate equation approach for our analysis.

Figure 4 shows the levels and rates considered. Levels a and b represent lower and upper state hyperfine levels coupled by a monochromatic laser, while level c is a trap level coupled radiatively to level b , but not to level a . In the absence of collisions, levels a and c effectively exchange population via transit relaxation. In cesium, a and c are the $F = 3$ and $F = 4$ (or $F = 4$ and $F = 3$, depending on which level is coupled by the laser) ground-state hyperfine levels, respectively. For homogeneously broadened transitions, we can write the following steady state rate equations:

$$\dot{n}_a = B_{ba} I_{r,y} \left(n_b - \frac{g_b}{g_a} n_a \right) - \Gamma_{ac} n_a + \Gamma_{ba} n_b + \Gamma_{ca} n_c = 0 \quad (1)$$

$$\dot{n}_b = -B_{ba} I_{r,y} \left(n_b - \frac{g_b}{g_a} n_a \right) - (\Gamma_{ba} + \Gamma_{bc}) n_b = 0 \quad (2)$$

$$\dot{n}_c = \Gamma_{ac} n_a + \Gamma_{bc} n_b - \Gamma_{ca} n_c = 0 \quad (3)$$

$$n_a + n_b + n_c = n. \quad (4)$$

Here, n is the total cesium atom density, n_i and \dot{n}_i are the density of the i th level and its time rate of change, respectively (note that in steady state $\dot{n}_i = 0$), Γ_{ij} is the population decay rate from level i to level j , and g_i is the degeneracy of the i th level. Also, $B_{ba} I_{r,y}$ is the stimulated emission rate, where B_{ba} is the Einstein coefficient and $I_{r,y}$ is the laser intensity incident upon position (r, y) in the cylindrical cell (where $r \equiv \sqrt{x^2 + z^2}$ is the radial distance from the laser beam axis and y is the position along the axis). When pumping a homogeneously broadened transition at line centre, the net absorption coefficient α_{hom} is

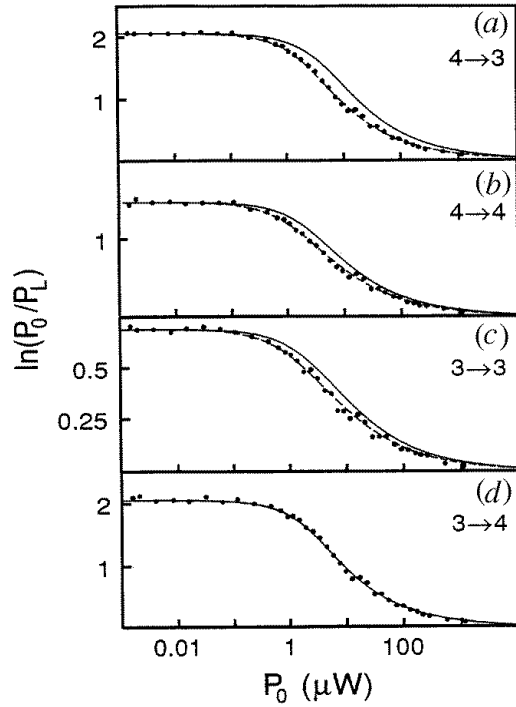


Figure 3. Effective line centre optical depth $\ln(P_0/P_L)$ against incident power P_0 . Each of the four $6S_{1/2}(F) \rightarrow 6P_{1/2}(F')$ hyperfine transitions (labelled as $F \rightarrow F'$) were analysed using data collected in set no 2. The magnetic field transverse to the laser polarization direction was $B_x = (0 \pm 5)$ mG. The experimental data appear as circles, while the results of the three-level model presented in section 3.1 of the paper appear as full curves. Note the lack of agreement between experiment and theory in some of the cases. Results of the multilevel theory presented in section 3.3 (broken curves) are in good agreement with experiment in all four cases. Results from data set no 1 are comparable in all respects.

defined as

$$\begin{aligned} \alpha_{\text{hom}} &= \frac{hc}{\lambda} \left(\frac{g_b}{g_a} n_a - n_b \right) B_{ba} \\ &= \frac{\lambda^2 \Gamma_{ba}}{4\pi \delta} \left(\frac{g_b}{g_a} n_a - n_b \right). \end{aligned} \quad (5)$$

Here, h is Planck's constant, c is the speed of light, $\lambda = 894.6$ nm is the transition wavelength, and δ is the homogeneous linewidth (HWHM). By solving the rate equations in steady state and substituting into equation (5), we find

$$\alpha_{\text{hom}} = \frac{\alpha'_0}{1 + I_{r,y}/I_{\text{sat}}} \quad (6)$$

where α'_0 is a constant obtained by setting $n_a = (ng_a)/(g_a + g_c)$ and $n_b = 0$ in equation (5) and

$$I_{\text{sat}} = \frac{4\pi hc \delta \Gamma_b \Gamma_t}{\lambda^3 \Gamma_{ba} [\Gamma_t + (g_b/g_a)(\Gamma_{ca} + \Gamma_{bc})]}. \quad (7)$$

Here, the total transit relaxation rate is defined as $\Gamma_t = \Gamma_{ca} + \Gamma_{ac}$ and the fluorescence decay rate of level b (assumed to be much larger than the transit relaxation rate of the excited state) is defined as $\Gamma_b = \Gamma_{ba} + \Gamma_{bc}$. Neglecting collisional broadening and quenching, $\delta = \Gamma_b/2$ and $\Gamma_b = 2.86 \times 10^7 \text{ s}^{-1}$ [7]. The rates Γ_{ba} and Γ_{bc} are calculated by summing and reducing magnetic sublevel transition matrix elements [8].

The transit relaxation rates are found by assuming that, under our experimental conditions, the cesium atoms do not interact with one another or with impurity atoms. Hence, the average atom passes through the laser beam in a straight line path without colliding with any other atoms. The transit relaxation rate is defined as $\Gamma_t = \bar{v}/\bar{d}$, where

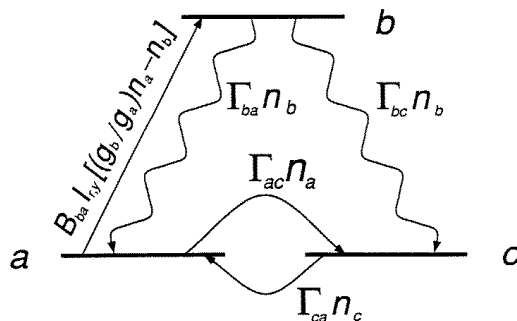


Figure 4. Population changing processes among the low lying cesium energy levels. Levels a and b represent the lower- and upper-state hyperfine levels coupled by a monochromatic laser, while level c is the remaining uncoupled ground-state hyperfine level for this excitation scheme. $\Gamma_{ij}n_i$ is the number of atoms (per cm^3) moving from level i to level j per unit time and $B_{ba}I_{r,y}((g_b/g_a)n_a - n_b)$ is the net number of atoms (per cm^3) pumped from level a to level b per unit time (absorption minus stimulated emission).

\bar{v} is the average atomic speed in two dimensions and \bar{d} is the average path length across the beam cross section. Assuming a two-dimensional Boltzmann distribution of velocities and a circular beam cross section (of diameter D), we find $\bar{v} = \sqrt{\pi kT/2m}$ and $\bar{d} = \pi D/4$ so that

$$\Gamma_t = \frac{\sqrt{8kT/\pi m}}{D} = 1.13 \frac{v_{\text{rms}}}{D} \quad (8)$$

where m is the cesium atomic mass, k is the Boltzmann constant, and $v_{\text{rms}} = \sqrt{2kT/m}$ is the two-dimensional root-mean-squared velocity. The derivation of equation (8) and discussion of the transit relaxation problem can be found in section 4.2. We also assume that atoms entering the beam are in a statistical mixture of the two ground-state hyperfine levels since, in this collision free model, such an atom last interacted with the cell walls. Hence, when an atom leaves the beam, this statistical population determines the probability that it is replaced by an atom in the other hyperfine level (a transit relaxation decay) or whether it is replaced by an atom in the same hyperfine level (no transit relaxation). Using this, the transit relaxation rates are

$$\Gamma_{ca} = \frac{g_c}{g_a + g_c} \Gamma_t \quad \Gamma_{ac} = \frac{g_a}{g_a + g_c} \Gamma_t. \quad (9)$$

Since the observed absorption lines are Doppler broadened, the effect of Doppler broadening on the theoretical absorption coefficient α_{hom} must be included in this model. A set of velocity dependent rate equations (similar to those in equations (1)–(3)) must be used to study the saturation of inhomogeneously (Doppler) broadened transitions [3,4]. Under these conditions, the absorption coefficient becomes

$$\alpha_{\text{Dop}} = \frac{\alpha_0}{\sqrt{1 + I_{r,y}/I_{\text{sat}}}} \quad (10)$$

with [9]

$$\alpha_0 = \sqrt{\frac{m}{128\pi^3 kT}} \lambda^3 \Gamma_{ba} \frac{g_b}{g_a + g_c} n. \quad (11)$$

Note that equations (10) and (11) are based upon an analysis that treats independently each velocity class within the Doppler broadened transition. At our vapour density, velocity-changing collisions, resonance exchange collisions, and radiation trapping are all sufficiently

infrequent that mixing among velocity classes within a single level can be considered negligible [10]. However, even at $T = 60\text{--}70^\circ\text{C}$, these effects become important.

The experiment discussed in section 2 measured the power of a Gaussian beam incident on the cesium cell, P_0 , and the power of this same beam after transmission through a length L of cesium vapour, P_L . The ratio of transmitted to incident intensity due to a vapour slab of thickness Δy , given by

$$\frac{I_{r,y+\Delta y}}{I_{r,y}} = e^{-\alpha_{\text{Dop}}\Delta y} \quad (12)$$

is intensity dependent due to the nonlinear absorption coefficient α_{Dop} . Since this intensity varies with both radius r (due to the Gaussian shape of the incident laser beam) and y (due to the attenuation of the beam power over the length of the cell), we must numerically calculate the transmitted power P_L . To do this, we divide the vapour into rings of radius r and thickness Δr . These rings have an incident intensity

$$I_{r,0} = I_{0,0} e^{-4 \ln 2 (r/D)^2} \quad (13)$$

where

$$I_{0,0} = \frac{4 \ln 2}{\pi D^2} P_0. \quad (14)$$

Then, this intensity is stepped through the vapour from $y = 0$ to $y = L$ (in 200 steps) using equation (12), thus yielding the transmitted intensity of this ring $I_{r,L}$. This process is repeated for rings (of thickness $\Delta r = D/100$) ranging from $r = 0$ to $r = 2D$, which are then summed using

$$P_L = 2\pi \int_0^\infty I_{r,L} r \, dr \approx 2\pi \sum_{j=1}^{200} (I_{j\Delta r,L}) j (\Delta r)^2 \quad (15)$$

to find the output power. The ratio $\ln(P_0/P_L)$ is calculated for many values of P_0 and then plotted as the full curves in figures 2 and 3. These plots are generated using no adjustable or fitted parameters (other than a slight adjustment of the total cesium density n , which is discussed in section 4.1). Note that this model agrees well with the data in all cases in figure 2, where $B_x = 1.1$ G, but that it is in poor agreement with the data for three of the four transitions in figure 3, where $B_x = 0$ G.

3.2. Multilevel model

The three-level model presented above is based upon a simple rate equation model which provides useful, and, in some cases, accurate predictions for the intensity dependent absorption of the D_1 line of cesium. However, it represents an oversimplification of the actual cesium atom. Hence, we also present a multilevel model which treats the $2F + 1$ distinct magnetic sublevels of each hyperfine level. As a result, neglected effects such as magnetic field mixing and population alignment are included.

Figure 5 shows the 32 magnetic sublevels that constitute the $6S_{1/2}$ and $6P_{1/2}$ states of cesium. Within each hyperfine level, the sublevels are considered to be distinct but degenerate in energy. A multilevel rate equation model, similar to the three-level model of the preceding section, is used. The multilevel model includes several effects that are not present in the three-level model. From equation (5), one can see that the pumping rate is proportional to the spontaneous emission rate between the two sublevels coupled by the laser. Since this pumping rate is different for each pair of coupled sublevels, a population alignment is generated across the sublevels of each hyperfine level. In addition, some sublevels of

level a are not coupled by the linearly polarized laser and therefore can trap population just like the sublevels of state c . This trapping further augments the population alignment within this state. These population aligning and trapping effects are offset somewhat by the population redistributing effects of transit relaxation. In this multilevel model, the transit relaxation rate is $\Gamma_t/16$ between each pair of sublevels within the $6S_{1/2}$ ($F = 3, 4$) states. Sublevel pumping and fluorescence decay rates are calculated using sublevel transition matrix elements from [8].

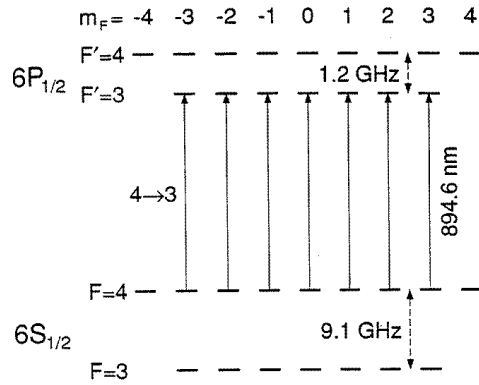


Figure 5. Magnetic sublevel and hyperfine structure of the cesium $6S_{1/2}$ and $6P_{1/2}$ states. Also shown are the sublevels coupled by a linearly polarized laser tuned to the $6S_{1/2}(F = 4) \rightarrow 6P_{1/2}(F' = 3)$ transition.

As in the three-level model, we set up a system of rate equations. However, there are now 23 or 25 coupled equations (depending on which pair of hyperfine levels are coupled by the laser). The coefficients of these equations were entered in numerical form (with the exception of incident intensity $I_{r,y}$, which was left as an unknown) into a matrix representing the coupled equations. This matrix then was diagonalized using Maple V. Steady state solutions for the populations of all sublevels were found by the Maple program in terms of $I_{r,y}$. Since all of the sublevel couplings within a transition occur simultaneously, an overall absorption coefficient is defined by summing up the individual sublevel absorption coefficients. Using equation (5), the total absorption coefficient is

$$\alpha_{\text{hom}} = \frac{\lambda^2}{4\pi\delta} \sum_{m_F=-F_<}^{F_<} \Gamma_{ba,m_F} (n_{a,m_F} - n_{b,m_F}) \quad (16)$$

where $F_<$ is the lesser of F_a and F_b , Γ_{ba,m_F} is the fluorescence decay rate between the two sublevels coupled by the laser, and n_{i,m_F} is the density of the sublevel m_F in state i . By proceeding analogously to the three-level model presented previously, the Doppler broadened line centre absorption coefficient is defined to be

$$\alpha_{\text{Dop}} \equiv \alpha_0 \sqrt{\frac{\alpha_{\text{hom}}}{\alpha'_0}}. \quad (17)$$

As before, the Gaussian transverse spatial profile of the laser beam and beam attenuation over the length of the cesium cell are included in this multilevel model using equations (12)–(15). Calculated values of this multilevel $\ln(P_0/P_L)$ are plotted as the broken curves against P_0 in figure 3. As before, these plots are generated using no adjustable parameters other than a slight adjustment of the total cesium number density n . Note the improved and excellent agreement with the data in all cases in figure 3.

It is important to note the physical source of the differences between the three-level and multilevel models. The primary failing of the three-level model is its inability to account properly for population trapped in state a sublevels. Hence, it overestimates the value of $\ln(P_0/P_L)$. The $F = 3 \rightarrow F' = 4$ excitation (figure 3(d)) has no such additional trap levels, so the three-level and multilevel model predictions are practically identical. The $4 \rightarrow 4$ (figure 3(b)) and $3 \rightarrow 3$ (figure 3(c)) excitations each have one unpumped state a sublevel (the $m_F = 0$ sublevel), leading to a discrepancy between the two theories. The $4 \rightarrow 3$ (figure 3(a)) excitation has two additional state a trap levels ($F = 4, m_F = \pm 4$), which produces even a larger difference between the three-level and multilevel model results.

3.3. Magnetic field effects

The multilevel model is used to predict the intensity dependent absorption for the data taken with a nonzero transverse magnetic field as well. To do this, the effects of magnetic field mixing must be included in the multilevel rate equation matrices. The magnetic field, applied perpendicular to both the laser propagation and polarization directions, causes a precession of the axis of atomic polarization \hat{z} about the direction of the applied field \hat{x} . This magnetic field induced depolarization is known as the Hanle effect [11] when detected by observing the polarization of spontaneously emitted fluorescence. In the \hat{z} basis, the population of a magnetic sublevel is redistributed among all of the magnetic sublevels within the hyperfine level by the transverse magnetic field B_x . Like transit relaxation, this population mixing within a hyperfine structure level offsets somewhat the population aligning and trapping effects discussed previously. However, at these low magnetic fields, it does not affect the overall rate of population transfer between ground-state hyperfine levels represented by Γ_1 . If the magnetic mixing rate is large enough, it can effectively eliminate population alignment and trapping in state a sublevels. Hence, the atom should behave like a three-level atom. This observation suggests that the transverse magnetic field applied in data sets no 3 and no 4 was large enough to create a vapour effectively composed of three-level atoms.

For the cesium $6S_{1/2}$ and $6P_{1/2}$ states (or any state where $J = 1/2$), the rate of precession of the laser polarization axis (or Larmor angular frequency) is given by [11]

$$\omega_L = \frac{g_J \mu_B B_x}{\hbar(2I + 1)} \quad (18)$$

where g_J is the Landé g -factor, μ_B is the Bohr magneton, and $I = 7/2$ is the nuclear spin quantum number for cesium. Based on this precession rate, we have set the rate of decay of population between a pair of magnetic sublevels due to magnetic mixing to be

$$\Gamma_m = \frac{g_J \mu_B B_x}{\hbar}. \quad (19)$$

This rate was inserted into the multilevel rate equation matrices.

If this magnetic mixing rate is going to generate effective three-level atoms, then it must be comparable to or larger than the fluorescence decay rates that generate the population alignment. These fluorescence rates are some fraction (as low as 1/48th) of the total $6P_{1/2} \rightarrow 6S_{1/2}$ transition fluorescence decay rate $\Gamma_b = 2.86 \times 10^7 \text{ s}^{-1}$. Using $B_x = 1.1 \text{ G}$, we find $\Gamma_m = 1.93 \times 10^7 \text{ s}^{-1}$. This rate appears to be large enough to sufficiently mix the population. By solving the multilevel rate equation matrices and plotting $\ln(P_0/P_L)$ versus P_0 , we generate results almost identical to those found by solving the three-level rate equations.

Also, the matrices were solved using a magnetic mixing rate of $\Gamma_m = 8.8 \times 10^4 \text{ s}^{-1}$. This corresponds to a transverse magnetic field of 5 mG, the maximum allowed at the cell

position by the experimental uncertainties in the zero field cases. To have a negligible effect upon the zero field results, this mixing rate should be much smaller than the transit relaxation rate, which was always greater than $\Gamma_t = 1.67 \times 10^5 \text{ s}^{-1}$ under our experimental conditions. As expected, this small magnetic mixing rate had no significant effect on the theoretical results obtained previously with no magnetic field.

4. Discussion

4.1. Assumptions and approximations

A sizable number of assumptions and approximations have been made in the theoretical analysis given above. Here, we will attempt to explain and justify them.

The cesium number density n is required for the calculation of α_0 in equation (11). This density is easily calculated using the cell temperature and the Nesmayanov vapour pressure formula [12]. However, due to the inaccuracy of our temperature measurement ($\pm 0.5^\circ\text{C}$) and of vapour pressure formulae in general, we expect a statistical and possibly a systematic uncertainty in our determination of the cesium number density (and hence α_0) of up to 5%. As expected, such a variation of α_0 was observed from experiment to experiment. A more accurate way of obtaining n is to use the low incident power data to find α_0 . The first five to eight data points were used from each of the four $\ln(P_0/P_L)$ against P_0 plots (see figures 2 and 3) to determine an experimental value for α_0 . Using other known constants in equation (11) allows us to calculate n for each point. Averaging these densities provides an accurate value of n necessary for the models.

In our models, we assumed that the effective radiative rate of the excited state was equal to the natural radiative rate, that the homogeneous linewidth was due to natural broadening only, and that the cesium atoms passed through the laser beam without interacting with any other particles. If the density of cesium atoms in the cell is too high, these approximations break down. Our measurements of α_0 (and the Nesmayanov vapour pressure formula) show that the cesium number density was $n \approx 4 \times 10^{10} \text{ cm}^{-3}$ at our experimental temperatures. This density is too small for radiation trapping to be significant ($< 3.5\%$ effect [10, 13]). Also, self-broadening does not significantly affect the homogeneous linewidth of the transition at this density [14]. In addition, long-range resonance exchange collisions with other cesium atoms limit the cesium atomic mean free path to several centimetres [10], but this is still much larger than the largest beam FWHM used in this experiment.

It is also known that the cesium vacuum cell used in this experiment has a background of impurity gases with density $n_{\text{im}} \leq 10^{14}$ [15]. However, this should not affect the approximations listed above. Using this impurity gas density and a typical upper limit to the quenching rate coefficient [16], we find that the quenching rate of cesium $6P_{1/2}$ atoms is negligible compared to that state's radiative rate. In addition, impurity gas broadening ($\Gamma = kn_{\text{im}}$ with a typical $k \approx 5 \times 10^{-9} \text{ cm}^3 \text{ s}^{-1}$) does not significantly influence the homogeneous linewidth compared to the natural width. Finally, the velocity-changing collision (VCC) rate between impurity gas molecules and cesium atoms may limit the cesium mean free path to as little as a centimetre using typical VCC rate coefficients [17]. We assume that the last interaction of a cesium atom entering the laser beam was with the cell walls, and therefore that these atoms are in a statistical ratio of ground-state hyperfine levels. Since the cell diameter is 2.1 cm, this assumption may not be strictly valid, but it is still a reasonable approximation.

It is well known that the temporal relaxation of excess population in state i due to transit relaxation does not have the general form $n_i(t) - n_i^{\text{eq}} = [n_i(0) - n_i^{\text{eq}}] e^{-\Gamma_{ij}t}$. In other

words, it is not entirely correct to describe transit relaxation by using a term $\Gamma_{ij}n_i$ in a rate equation model. The actual transit relaxation, shown in figure 6, cannot be represented by a simple exponential rate. Hence, the choice of an effective rate coefficient Γ_t (here set equal to the reciprocal of the average time of flight of an atom through the laser beam cross section) is somewhat arbitrary. Our value for the transit relaxation rate coefficient is compared to similar coefficients used by other researchers in the following subsection.

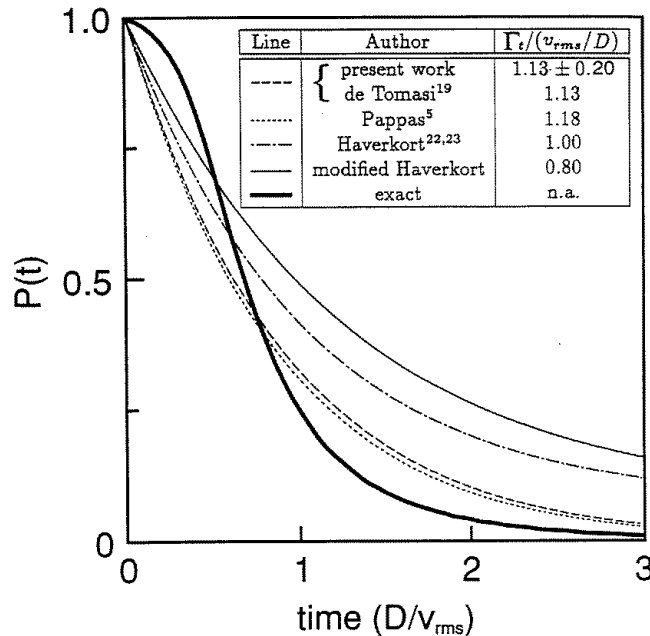


Figure 6. Transit relaxation. Given that a cesium atom enters the laser beam at time $t = 0$, the thick full curve shows the probability $P(t)$ of the atom still being within the beam at a later time t . This curve was found by averaging over all possible velocities (as given by a two-dimensional Boltzmann distribution of velocities) and trajectories across a circle to find atomic flight times through the beam profile. The units of time are D/v_{rms} , where D is the FWHM of the Gaussian beam and v_{rms} is the two-dimensional root-mean-squared atomic velocity. The other lines are plots of $P(t) = e^{-\Gamma_t t}$, where Γ_t is the effective transit relaxation rate. These effective rates are discussed in the text (section 4.2) and listed in the insert. The rate Γ_t is simply the numerical coefficient listed, times v_{rms}/D .

Another approximation made concerning transit relaxation involves the general idea of an atom passing through an interaction region of circular cross section with diameter D . We assume that the atom interacts with the laser within a circular area of diameter D and does not interact beyond this circle. Since the laser beam spatial profile is Gaussian, the choice of D equal to the Gaussian FWHM is somewhat arbitrary. In addition, attenuation of the low-intensity spatial wings is much more severe than attenuation of the highly saturated beam centre. Thus, the beam shape is distorted and the beam diameter effectively decreases with depth into the vapour. Here, we calculate the transit relaxation rate using the incident beam FWHM, D . However, the good agreement between the model and the experimental data appears to justify this approximation.

Our models have neglected the sublevel splitting produced by the magnetic field. The splitting (in angular frequency units) of adjacent ground-state magnetic sublevels (i.e. $\Delta m_F = \pm 1$) in the \hat{x} basis due to the magnetic field $B_x = 1.1$ G is given by the Larmor

frequency ω_L defined by equation (18). This splitting is much less than the homogeneous width δ of each sublevel transition. Hence, the assumption that the sublevels within a particular hyperfine state are degenerate, which is implicit in the multilevel model, is a good one.

As with transit relaxation, the temporal decay of population from sublevel i due to magnetic mixing is non-exponential. However, we again approximate it as such to incorporate it easily into the rate equation model. The magnetic mixing of population among the m_F sublevels (defined in reference to the z axis) is a result of the precession of the atomic polarization axis around the x axis. The temporal redistribution of population is found by using rotation matrix elements [18] to project the rotated axis of polarization onto the z axis. After a time $1/\Gamma_m$, we observed (via numerical simulation) that population oscillates among the sublevels within each hyperfine level at frequencies $\omega = \omega_L, 2\omega_L, \dots, 2F\omega_L$. Hence, it seems reasonable to set a magnetic mixing rate of decay of population out of a particular sublevel as $\Gamma_m = \omega_L(2I + 1) = g_J\mu_B B_x/\hbar$. Unfortunately, this experiment cannot determine the quality of this approximation because our data were obtained in the limits of no mixing ($B = 0$ G) and complete mixing ($B = 1.1$ G).

4.2. Effective transit relaxation rate coefficients

The quality of the agreement between the modelled curves and experimental data points in figures 2 and 3 allows us to place limits on the value of the effective transit relaxation rate coefficient. We are able to do this because all other rates in the model depend on well known or accurately measured physical quantities. Hence, the quality of the model reflects the quality of the combination of approximations used to describe transit relaxation. By varying the effective transit relaxation rate coefficient Γ_t in the model, and comparing the generated curves with the data, we estimate the uncertainty in this calculated rate to be $\pm 18\%$.

The value used here for the effective transit relaxation rate coefficient was defined by $\Gamma_t = \bar{v}/\bar{d}$. Here, the average speed \bar{v} is

$$\bar{v} = \int_0^\infty v P(v) d^2v = \sqrt{\frac{\pi kT}{2m}} \quad (20)$$

where $d^2v = 2\pi v dv$ and

$$P(v) = \frac{e^{-(v/v_{\text{rms}})^2}}{\pi v_{\text{rms}}^2} \quad (21)$$

is the normalized two-dimensional Boltzmann distribution. The average distance \bar{d} is found by averaging all possible paths through a circle representing the laser beam cross section. For simplicity, we consider only atoms travelling parallel to the z axis. Hence,

$$\bar{d} = \frac{2}{D} \int_{-D/2}^{D/2} dx \sqrt{(D/2)^2 - x^2} = \frac{\pi}{4} D. \quad (22)$$

Using equations (20) and (22) and the uncertainty quoted above, the effective transit relaxation rate coefficient becomes

$$\Gamma_t = (1.13 \pm 0.20) \frac{v_{\text{rms}}}{D}. \quad (23)$$

This value can be compared to the results obtained by other researchers using different approaches to this problem.

One approach to this problem was formulated by de Tomasi [19], but has not been published. He considered a homogeneous distribution of n atoms located at random positions (r, θ) and moving in random directions θ' within a circular beam cross section of radius R . The transit relaxation rate was found by considering the number of atoms leaving this circle (Δn) in a short time (Δt). Hence,

$$\Delta n = n \int_0^{2\pi} \int_0^R \frac{r \, dr \, d\theta}{\pi R^2} \int_0^{2\pi} d\theta' \int_{r'/\Delta t}^{\infty} P(v) v \, dv \quad (24)$$

where

$$r' = r \cos \theta' + \sqrt{R^2 - (r \sin \theta')^2} \quad (25)$$

is the distance from an atom's position (r, θ) to the edge of the circle in the direction θ' . Equation (24) was integrated numerically to find Δn . The rate coefficient is defined by

$$\Gamma_t = \frac{dn/dt}{n} = \frac{1}{n} \lim_{\Delta t \rightarrow 0} \frac{\Delta n}{\Delta t} = 1.13 \frac{v_{\text{rms}}}{D} \quad (26)$$

where the last step is found by taking the limit $\Delta t \rightarrow 0$ of the numerical results. De Tomasi's result is identical to that obtained in the present work.

Pappas *et al* [5] use a rate coefficient of $\Gamma_t = \sqrt{2} v_{\text{rms}} / D_{1/e} = 1.18 v_{\text{rms}} / D$ (where $D_{1/e}$ is the Gaussian beam $\text{FW}_{\frac{1}{e}}\text{M}$), although they do not provide either a derivation or a reference for this result. However, the same value was shown previously by Bordé *et al* [20] to be the frequency $\text{HW}_{\frac{1}{e}}\text{M}$ of a (non-Lorentzian) transit time broadened line profile and subsequently quoted in [21] as a transit relaxation rate, although the equality of this linewidth and the transit relaxation rate is not discussed in these references. Nonetheless, the resulting rate coefficient agrees within uncertainty with the rates calculated and measured here. (We note here that Bordé *et al* predict an exponential lineshape for a transition broadened purely by transit time broadening. In our case, $\Gamma_b \gg \Gamma_t$, so that the lineshape here should be well described by a Voigt convolution of a Doppler-broadened Gaussian and a homogeneously-broadened Lorentzian.)

In [22, 23], the authors (Haverkort *et al*) use the low-density limit of a diffusion rate coefficient to find the transit relaxation rate. The authors quote this limit as $\Gamma_t = v_{\text{rms}} / 2R$. This equation yields $\Gamma_t = v_{\text{rms}} / D$, assuming that the beam radius R from their paper is the Gaussian beam HWHM. This barely agrees with our experimental and theoretical results within uncertainty. However, in re-examining the limiting case of the same diffusion equation, we find the result to be $\Gamma_t = 0.8 v_{\text{rms}} / 2R$. This clearly does not agree with our result within its uncertainty. Thus, we believe that the method of finding the transit relaxation rate in [22, 23] produces results that slightly underestimate the observed rate.

Figure 6 lists all of the results of the transit relaxation rates calculated. Note that two of the approaches yield the same result, while a third agrees well within experimental uncertainty. However, as can be seen in the figure, the exponential population decay represented by these rate coefficients is only a very crude approximation to the actual non-exponential transit relaxation decay. Nonetheless, we believe the present experiment shows that equation (23) represents the best expression for a transit relaxation rate for use in a rate equation model.

As mentioned previously, we have modelled the Gaussian spatial profile of the laser beam with a circle of diameter D equal to the FWHM of the beam intensity distribution for the purpose of calculating effective transit relaxation rate coefficients. This model generated the curves shown in figures 2 and 3. If instead, the $\text{FW}_{\frac{1}{e}}\text{M}$ was used for the beam diameter, the calculated value of Γ_t would be reduced by 17%. This would shift the model curves of figures 2 and 3 to the left such that the half maximum point (i.e. the value of P_0 for which

$\ln(P_0/P_L)$ is equal to half of its maximum value) would be reduced by approximately the same amount. Thus, calculation of the transit relaxation rate using the $\text{FW}_{\frac{1}{e}}M$ for the beam diameter produces results that differ from experiment by slightly less than the experimental uncertainties. Hence, although our data favour the use of the beam profile FWHM in the calculation of Γ_t , they are not sufficiently accurate to exclude the use of the Gaussian beam $\text{FW}_{\frac{1}{e}}M$.

5. Conclusions

Saturation of atomic transitions is easily observed using tunable narrow-band lasers. When trap atomic levels are available, this saturation may be observed at relatively low intensities. However, accurately modelling the intensity dependent absorption of a real atomic transition is not necessarily a simple task, even under ideal conditions (i.e. one isotope, no overlapping hyperfine transitions, low density, low temperature) such as those available in this experiment involving the cesium D_1 line. A three-level model provides effective predictions in some cases, but generally, a more complex multilevel model that includes all of the magnetic sublevels is required. Using this multilevel model, we can reproduce all of the data presented. Also, accurate modelling of transit relaxation and, in the presence of a magnetic field, of magnetic sublevel mixing is necessary. Here, we have found that an effective transit relaxation rate coefficient of $\Gamma_t = (1.13 \pm 0.20)v_{\text{rms}}/D$ is required to accurately model our data. This model could be adjusted to accommodate diffusion, collisional effects, and the hyperfine structure to study saturation of other transitions at higher densities with and without buffer gases. The approach used here may also be extended to model more complex nonlinear phenomena, such as optical bistability, two beam coupling, or four-wave mixing based upon nonlinear absorption phenomena in real atoms.

Acknowledgments

The authors would like to thank Drs Alan Streater, Michelle Malcuit, A Peet Hickman, and Ferdinando de Tomasi for many valuable discussions on this topic. We would also like to thank Amy Perkins for her assistance in the early phases of this project and Dr George Watkins for the use of the Gaussmeter. We would like to acknowledge financial support for this work from the National Science Foundation under grant No PHY-9119498.

References

- [1] Boyd R W 1992 *Nonlinear Optics* (San Diego, CA: Academic)
- [2] Butcher P N and Cotter D 1990 *The Elements of Nonlinear Optics* (Cambridge: Cambridge University Press)
- [3] Yariv A 1989 *Quantum Electronics* (New York: Wiley)
- [4] Demtröder W 1981 *Laser Spectroscopy* (Berlin: Springer)
- [5] Pappas P G, Burns M M, Hinshelwood D D, Feld M S and Murnick D E 1980 *Phys. Rev. A* **21** 1955
- [6] Akulshin A M, Sautenkov V A, Velichansky V L, Zibrov A S and Zverkov M V 1990 *Opt. Comm.* **77** 295
- [7] Rafac R J, Tanner C E, Livingston A E, Kukla K W, Berry H G and Kurtz C A 1994 *Phys. Rev. A* **50** R1976
- [8] Condon E U and Shortley G H 1971 *The Theory of Atomic Spectra* (Cambridge: Cambridge University Press)
- [9] Mitchell A C G and Zemansky M W 1935 *Resonance Radiation and Excited Atoms* (Cambridge: Cambridge University Press)
- [10] Huennekens J, Namiotka R K, Sagle J, Jabbour Z J and Allegrini M 1995 *Phys. Rev. A* **51** 4472
- [11] Corney A 1977 *Atomic and Laser Spectroscopy* (Oxford: Clarendon)
- [12] Nesmayanov A N 1964 *Vapour Pressure of the Elements* (New York: Academic)
- [13] Colbert T and Huennekens J 1990 *Phys. Rev. A* **41** 6145
- [14] Jabbour Z J, Sagle J, Namiotka R K and Huennekens J 1995 *J. Quant. Spectrosc. Radiat. Transfer* **54** 767

- [15] Jabbour Z J, Namiotka R K, Huennekens J, Allegrini M, Milošević S and de Tomasi F 1996 *Phys. Rev. A* submitted
- [16] Tanarro I, Arqueros F and Campos J 1982 *J. Phys. B: At. Mol. Phys.* **15** 1826
- [17] Liao P F, Bjorkholm J E and Berman P R 1980 *Phys. Rev. A* **21** 1927
- [18] Rose M E 1957 *Elementary Theory of Angular Momentum* (New York: Wiley)
- [19] de Tomasi F, private communication
- [20] Bordé C J, Hall J L, Kunaşz C V and Hummer D G 1976 *Phys. Rev. A* **14** 236
- [21] Thomas J E and Quivers W W Jr 1980 *Phys. Rev. A* **22** 2115
- [22] Haverkort J E M, Werij H G C and Woerdman J P 1988 *Phys. Rev. A* **38** 4054
- [23] Haverkort J E M 1987 *PhD Thesis* Leiden University (unpublished)